

## MICRO INTERFEROMETER BASED ON AMORPHOUS SILICON NANOSENSOR

E. Bunte, K. H. Jun, H. Stiebig\*

Institute of Photovoltaics, Research Center Jülich, D-52425 Jülich, Germany

Length measurement with nm-accuracy can be carried out by means of a new phase selective partly transparent detector (PSTD). The working principle bases on the sampling of a standing wave created in front of a movable mirror. The pivotal element of the set-up is the developed nanosensor - a thin stack of two almost transparent photodiodes of amorphous silicon deposited on a glass substrate. The two photodiodes measure the intensity of an optical standing wave by means of absorption layers with thicknesses below 50 nm and thus, provide two photocurrents which are proportional to the intensity at their individual positions. The design of the multi layer stack has to be optimized regarding high transmittance, minimized distortions of the standing wave, and a phase shift of 90° between the photocurrents of the two diodes. Different concepts to adjust the phase shift between the photocurrents of the two diodes without deteriorating the other conditions were studied by means of optical simulations. Lissajous figures close to a perfect circle are recorded to demonstrate the operation principle of the new device. Further aspects to improve the performance of the PSTD will be discussed.

(Received May 19, 2005; accepted July 21, 2005)

*Keywords:* Micro interferometer, Amorphous silicon, Nanosensor

### 1. Introduction

Length measurement and position detection in the nm-range is important in coordinate measuring systems, lithographers and position calibrators [1]. For these tasks laser interferometers are commonly used, since they offer a high measurement precision. The state-of-the-art technology is the Michelson interferometer. We have realized an alternative, a so-called standing wave interferometer for length measurements, which utilizes the existence of an optical standing wave in front of a plane mirror. This nanosensor set-up has the potential to substitute the Michelson interferometer as a more inexpensive and compact alternative. The utilization of an optical standing wave for length measurement was investigated in the past [2, 3, 4], but our approach reduces the number of optical components to a minimum. Another interesting application of optical standing waves are Fourier spectrometers [5,6,7]. Based on a linear arrangement of a transparent detector and the mirror, the spectrometer facilitates the realization of one- and two dimensional arrays of spectrometers combining spectral and spatial resolution. The spectral information of the incoming light can be determined by the Fourier transform of the photocurrent measured by the transparent detectors.

An optical standing wave can be generated by a laser, e.g. a He-Ne laser with a wavelength ( $\lambda$ ) of 633 nm, which is orthogonally incident onto a mirror. This set-up leads to an interference of two electromagnetic waves propagating in opposite direction forming. The standing wave is characterized by its intensity profile  $I$ . The intensity of an ideal optical standing wave (no light distortion by the detector) is proportional to the square of the electrical field  $E$  of the wave (Eq. 1).

$$I(z) \propto E_z^2 + E_{-z}^2 - 2E_z E_{-z} \cos(2kz) \quad \text{with } k = 2\pi / \lambda \quad (1)$$

---

\* Corresponding author: h.stiebig@fz-juelich.de

$E_z$  and  $E_{-z}$  describe the incident wave and the wave that has been reflected at the mirror, respectively. I consists of minima and maxima which appear with a distance of  $\lambda/(2n)$ .  $n$  is the optical constant of the employed material. Since the waves propagate in material with different optical constants (air, glass, TCO, a-Si:H) the period of the standing wave varies. At the mirror always occurs a minimum, since here the electric field disappears. Hence, the intensity profile is spatially fixed and can be shifted when the mirror is moved along the  $z$ -axis. By sampling the intensity with a partly transparent photodiode, information about the mirror displacement can be obtained. The task of the diode is to generate a photocurrent corresponding to the standing wave intensity at its position. Moving the mirror along the optical axis shifts the intensity profile through the photodiode. Consequently a mirror-position-dependent photocurrent is generated in the device.

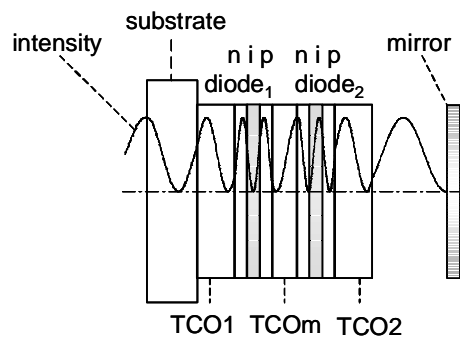


Fig. 1. Sketch of a new micro interferometer based on a nanosensor of a-Si:H.

However, with one diode the direction of the mirror movement cannot be determined. To identify the direction, two photodiodes must be implemented into the standing wave providing two independent photocurrents. Fig. 1 shows a sketch of an integrated detector concept. If the mirror is moved, two periodical photocurrents can be displayed on the  $x$ - and  $y$ -channel of an oscilloscope as a Lissajous (L) curve. Those can be evaluated for bi-directional fringe counting – a standard method for interferometrical length measurements. With this method the mirror displacement can be determined with an accuracy significantly shorter than the period of the standing wave.

For two sinusoidal photocurrents, the L-figures form ellipses. The shape of the ellipse depends on the phase shift ( $\gamma$ ) between the photocurrents. For  $\gamma = 0^\circ, 180^\circ, 360^\circ, \dots$  (the values will be simply referred as  $0^\circ$  from now on), the ellipse shrinks to a line and the direction of the mirror movement can not be determined. For  $\gamma$  of  $90^\circ, 270^\circ, 450^\circ, \dots$  (the values will be simply referred as  $90^\circ$  from now on), the L-figure depicts a circle and the two signals build an orthogonal system. These cases are desirable, since they are optimal for the least measurement error [8]. A deviation from  $\gamma = 90^\circ$  leads to an increase of the error. Furthermore, a deviation of the photocurrents from a sine function also increases the measurement error.

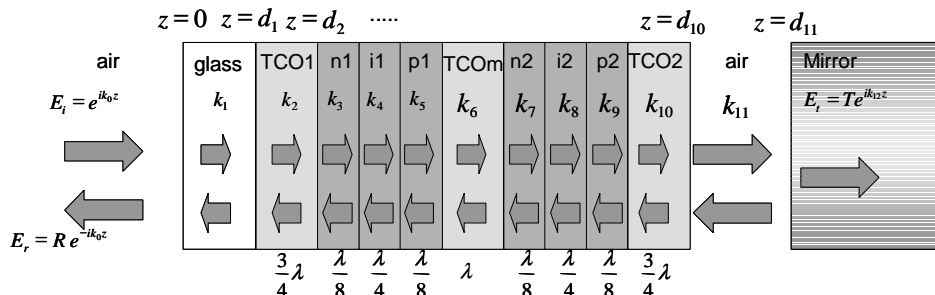


Fig. 2. Layer scheme of the simulated PSTD. An example of optimum thickness values for maximum transmission are displayed in this figure. Note, in this case, the  $\lambda$  values represent the wavelength in each material. For example,  $\lambda$  in TCO is  $\lambda_{air}/n_{TCO}$ , where  $n_{TCO}$  denotes the refractive index of TCO. Therefore the thicknesses of layers are; TCO1: 250 nm, n1: 22 nm, i1: 44 nm, p1: 23 nm, TCO m: 333 nm, n2: 22 nm, i2: 44 nm, p2: 23 nm, and TCO2: 250 nm.

We have developed a nanosensor consisting of two stacked n-i-p photodiodes with an absorption layer thickness shorter than  $\lambda$  of the incident light. The two diodes of the phase selective partly transparent detector (PSTD) are embedded between three transparent conductive oxide (TCO) contact layers which border the amorphous silicon (a-Si:H) n-i-p diodes (see Fig. 2). Such devices can be used to sample the intensity profile of a standing wave and have proven to deliver two independent photocurrents enabling bi-directional fringe counting [9]. The measured photocurrents of the fabricated PSTD do not describe pure sine functions but show distortions, which increase the measurement error [10]. The optoelectronic properties of a single n-i-p diode and a PSTD based on experimental studies are discussed elsewhere [11, 12]. We have performed simulations to optimize the device layer structure so that the phase difference between the photocurrents of the diodes is close to  $90^\circ$  and the photocurrents show almost sinusoidal behavior. Based on a comparison of simulated and measured photocurrents the working principle of the PSTD will be discussed in detail and further optimization criteria will be outlined.

## 2. Experiment

The nanosensors were deposited on a  $10 \times 10 \text{ cm}^2$  Corning glass, type 1737F with a thickness of around 1.1 mm (0.48 inch). For the fabrication of the devices we took benefit from the well-developed a-Si:H based thin-film process for solar cells [13]. The preparation of the TCO layers was performed by rf-magnetron sputtering of aluminum doped zinc oxide (ZnO) and the amorphous silicon layers were deposited in a multi-chamber PECVD system at  $210^\circ\text{C}$  as an n-i-p layer sequence.

Assuming that the charge carriers generated in the p- and n-layer do not contribute to the photocurrent, the i-layer represents the absorber layer. It was prepared using a gas mixture of silane, methane and hydrogen. Thus, it is composed of amorphous silicon carbide (a-SiC:H) and has an optical band gap of  $E_g = 2.0 \text{ eV}$ . The p-layer was deposited with a-SiC:H ( $E_g = 1.9 \text{ eV}$ ), whereas the n-layer consists of a-Si:H ( $E_g = 1.75 \text{ eV}$ ). p- and n-type doping were performed by adding trimethylboron and phosphine to the process gases, respectively. The deposition procedure has a reproducibility of the layer thickness of approximately  $\pm 5 - 10 \text{ nm}$ .

A critical issue represents the deposition conditions of the TCO layers. Since the thickness of the amorphous layer system is below  $100 \text{ nm}$ , special efforts were attempted to avoid shunt problems, e.g. the sputtering rate for TCO2 and TCOm was decreased to keep the kinetic energy of the striking particles low. TCO2 and TCOm were sputtered at room temperature (RT) to prevent a damage of the underlying amorphous layer system. In order to achieve a high conductivity for TCO1 the layer is prepared at a heater temperature of  $400^\circ\text{C}$ . The specific resistance of a ZnO-layer nearly linearly decreases with the temperature. Since the TCO1 and TCO2 layer act as anti reflection coating their thickness must be equal to an uneven multiple of  $\lambda/(4n_{\text{TCO}})$ . In the simplest case ( $d_{\text{TCO}} = \lambda/(4n_{\text{TCO}})$ ), the TCO layers have a thickness of only  $80 \text{ nm}$ . For these ZnO layers a specific resistance of around  $2.8 \times 10^{-3} \Omega\text{cm}$  and a  $R_{\text{square}}$  of around  $300 \Omega/\square$  was achieved if deposited at RT. Due to the different sputtering conditions, e.g. higher temperature, the employed TCO1 layer has a  $R_{\text{square}}$  of around  $15-19 \Omega/\square$  which is around five times lower than for the TCO2 layers. As a compromise between a low resistance and consequently a high cut-off frequency, a high yield of shunt-free devices and a good optical adjustment a thickness of  $240 \text{ nm}$  was chosen for the TCO1 and TCO2 layers. The reproducibility of the TCO layer thickness is in the range of  $\pm 20 \text{ nm}$ . More details regarding the optoelectronic properties of the rf-sputtered ZnO is given elsewhere [14].

$\gamma$  between the photocurrents is determined by the design of the layer stack, e.g. the layer thicknesses, refractive indices, etc. A proper layer scheme to achieve the aimed  $\gamma$  of  $90^\circ$  will be discussed later on. The detectors were patterned using photolithography and reactive ion etching. The first-deposited diode 1 has an area of  $10.7 \text{ mm}^2$ , while diode 2 is slightly smaller ( $8.9 \text{ mm}^2$ ) to enable a contacting of the underlying diode 1. The photocurrent measurements within the standing wave were performed using a stabilized He-Ne laser ( $\lambda_{\text{air}} = 633 \text{ nm}$ ) with a power of  $0.92 \text{ mW}$ .

## 3. Model

Modelling can be a useful tool for the device analysis, because the relatively high absorption coefficients of the layers make a conceptual prediction of the standing waves within the

device difficult. Thus, a detailed electromagnetic simulation of the device is performed in order to achieve a better understanding of the wave propagation through the multi-layer stack and to develop further optimization criteria. A sketch of the PSTD based on a glass/TCO1/n-i-p/TCOm/n-i-p/TCO2 nanosensor shows Fig. 2. To simulate this structure, we assumed a plane wave which normally impinges (TEM mode) on the glass side. The time dependence  $\exp(-i\omega t)$  is assumed for the electric field. In Figure 2,  $k_j$  is the wave number in the  $j$ th region. The incident electric field has the unit amplitude.  $R$  is the reflectance and  $T$  is the transmittance. We considered silver as a non-ideal mirror. The electric field (x component) in the  $j$ th region is

$$E_j = E_j(d_{j-1})\exp[ik_j(z - d_{j-1})] + E_j(d_j)\exp[-ik_j(z - d_j)] \quad (2)$$

The coefficients  $E_j(d_{j-1})$  and  $E_j(d_j)$  represent the amplitudes of the right-going and the left-going fields in the  $j$ th region, respectively. The absorbance of the individual i-layer can be calculated according to [15] by the following equations:

$$A_{\text{diode1}} = \text{Re}\left\{\frac{E_4(d_4)H_4^*(d_4) - E_4(d_3)H_4^*(d_3)}{E_i(0)H_i^*(0)}\right\} \quad (3a)$$

$$A_{\text{diode2}} = \text{Re}\left\{\frac{E_8(d_8)H_8^*(d_8) - E_8(d_7)H_8^*(d_7)}{E_i(0)H_i^*(0)}\right\} \quad (3b)$$

The direction of the E and H fields was chosen to match the propagation of the TEM wave. The absorbance is normalized by the incident wave. The magnetic field is obtained from the Maxwell's curl equation, assuming that the media are nonmagnetic. The coefficients  $E_j(d_{j-1})$  and  $E_j(d_j)$  are determined by means of a matrix formalism [16]. This approach correlates the input and the output electric field vectors of the whole layer stack by a linear function and enables the determination of the coefficients at each interface in an iterative way.

Assuming that the photocurrent in each diode can only be attributed to the absorbed light in the i-layer, the absorbance of the i-layer is proportional to the photocurrent. Thus, absorbance and photocurrent can be used synonymously. In the following, the wave form within the device will be discussed by the absorbance of the diodes. We deduced the dielectric functions of the layers by measuring the transmittance (T) and the reflectance (R) of individual thin films deposited on the glass substrate. We also determined the growth rate of each layer by this method. We calculated the photocurrent as a function of the mirror-position. Initially the mirror was assumed to be placed 10 cm behind the device ( $d_{10} + 10 \text{ cm} = d_{11}$ ). The simulations were carried out for an increased air gap up to  $d_{10} + 10 \text{ cm} + 633 \text{ nm} = d_{11}$ . The displayed phase shift value was obtained by fitting the curves by ideal sine functions and determining the phase difference between the two sine functions. The aim was to design a layer stack, which yield photocurrents with low distortions and a  $\gamma$  close to  $90^\circ$ .

#### 4. Simulation

One prerequisite to receive distortion-free photocurrents is the minimization of internal reflections. A way to achieve this is to ensure high transparency of the device at  $\lambda_{\text{air}}$  of the laser light. Thus, a layer stack which shows highest possible T has to be designed. Fig. 2 contains possible layer thicknesses for maximum transparency. The total thickness of the device is a multiple of  $\lambda$  and the TCO1 and TCO2 act as anti reflection coatings. For a layer system with no absorption and no internal reflections,  $\gamma$  between the photocurrents is determined by the distance between the centers of the two i-layers, which is given by the sum of  $i1/2$ ,  $p1$ , TCOm,  $n2$ , and  $i2/2$ . However, the thickness values as given in Fig. 2 result in a  $\gamma$  of  $540^\circ$ , which corresponds to a multiple of  $\lambda/2$ . Thus, the shape of the L-curve shrinks to a single line (will be discussed with Fig. 4) and the direction of the mirror movement can not be determined.

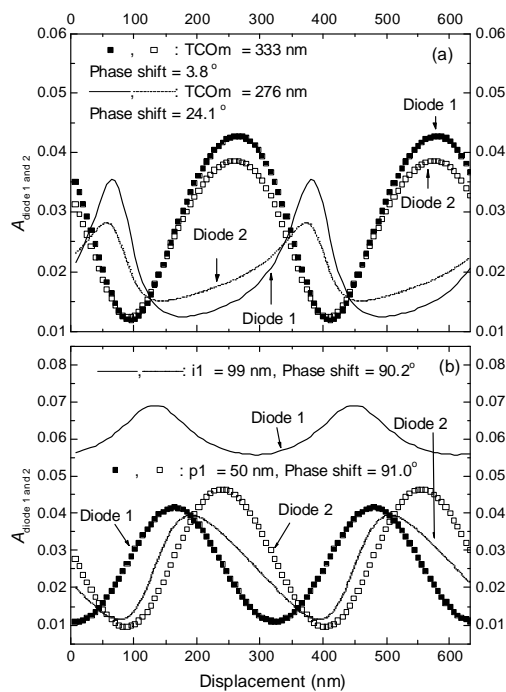


Fig. 3 (a). Simulated absorbance of Diode 1 and 2 with different TCOM thicknesses and (b) with increased  $i1$  and  $p1$  layer thickness. The other layer thicknesses are kept constant as given in Fig. 2.

In the following numerical simulations the dielectric functions  $n$  and  $\kappa$  of each individual layer have been taken into account to study their influence on the wave propagation within the thin-film layer stack. The glass thickness was set to 1.117556 mm (0.48 inch). Fig. 3 (a) and (b) show the simulated absorbances  $A_{diode1}$  and  $A_{diode2}$  and Fig. 4 shows the corresponding L-curves. In Figs. 3 (a) and (b), the differences of the direct current (DC) levels and the amplitudes between the two diodes are attributed to the slightly higher light absorption in the diode 1. A mirror displacement of 633 nm results in a photocurrent (represented by the absorbance) that displays two intensity periods. In Fig. 4, for clear comparison of the shapes, we removed the DC parts and normalized the alternating current (AC) signals to vary within -0.5 and 0.5.

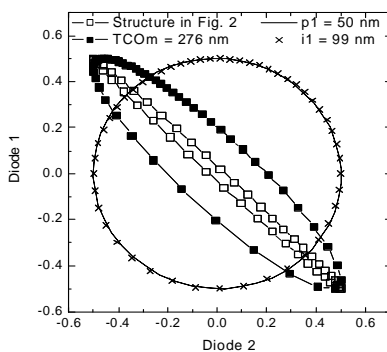


Fig. 4. Corresponding Lissajous figures to the calculated photocurrents shown in Fig. 3.

The simulation of the layer structure in Fig. 2 is shown in Fig. 3 (a) and Fig. 4. The corresponding L-curve almost shrinks to a single line.  $\gamma$  of the two photocurrents results to  $3.8^\circ$ . A phase of  $0^\circ$  can not be observed, since the absorption in the layers was taken into account and has an influence on the phase shift. To obtain the desired  $\gamma$  of  $90^\circ$ , the thicknesses of the individual layers have to be changed. In the following, we discuss three different cases. We have changed the thickness of (i) TCOm layer (ii) p1-layer and (iii) i1-layer, while the other layers were kept constant with values as denoted in Fig. 2. That means, the proposed variations of the layer thicknesses result in a deviation from the total optical layer thickness of a multiple of  $\lambda$  for an ideal device.

Let's first focus on changing the TCOm layer. From the simple point of view – neglecting absorption and internal reflections – a  $\gamma$  of  $90^\circ$  might be reached for a TCOm layer of  $\lambda_{\text{TCO}} - \lambda_{\text{TCO}}/8 = 7\lambda_{\text{TCO}}/8$  thickness. However, the simulations considering absorption and internal reflections reveal that the phase shift of  $90^\circ$  cannot be implemented by any change of the TCOm layer thickness. Fig. 3 (a) shows the simulated photocurrents for a TCOm layer of 276 nm ( $\sim 0.83\lambda_{\text{TCO}}$ ). Fig. 4 depicts the corresponding L-curves.  $\gamma$  between the photocurrents is  $24.1^\circ$ . This is the highest  $\gamma$  that can be reached by varying the TCOm layer thickness. Also the wave forms are significantly distorted in this case. Due to the absorption in the TCO layers and internal reflections at the TCO/a-Si:H interfaces, a variation of the TCO layers strongly affects the wave propagation. Thus, a change of the TCOm layer is no mean to adjust a  $\gamma$  of  $90^\circ$ .

Next, we have modified the p1 layer to  $p1 = 0.27\lambda_{\text{a-SiC:H}}$  (50 nm) keeping the other parameters as in Fig. 2. Fig. 3 (b) shows the simulated absorbance. The corresponding L-curves are given in Fig. 4. Increasing the p1 layer enables the realization of our goal: sine shaped photocurrents and a  $\gamma$  close to  $90^\circ$ . Note that instead of varying the p1 (a-SiC:H) layer also a variation of the n2-layer (a-Si:H) can lead to a  $\gamma$  near  $90^\circ$ . However, the former solution is more preferable due to the lower absorption losses within the carbon alloyed layer.

Finally, we have varied the i1-layer to  $i1 = 0.57\lambda_{\text{a-Si:H}}$  (99 nm) keeping the other parameters as in Fig. 2. This leads to  $\gamma = 90.2^\circ$ . However the calculated absorbance is significantly distorted (Fig. 3 (b)). A further disadvantage is the increase of the DC part and the slight reduction of the AC part of the photocurrents [12, 17]. The DC component is determined by the first and second term of eq. 1. Since the absorption coefficient of a-Si:H at  $\lambda = 633$  nm is very small, the DC component is nearly linearly proportional to the i-layer thickness. With increasing i-layer thickness the AC/DC ratio decreases and, consequently, the noise to signal ratio elevates. The simulations show that a successful strategy to reach a  $\gamma$  of  $90^\circ$  and nearly undistorted sinusoidal photocurrents can base on an increase of the p1-layer thickness.

## 5. Results and discussion

Based on the above-presented concept we have prepared PSTD with a thickness scheme according to Fig. 2 but with an enlarged p1-layer by around 20 nm to reach the aimed phase difference of  $90^\circ$ . Fig. 5 exhibits the measured R and T curves of the fabricated thin-film device. At  $\lambda = 610$  nm the interference pattern exhibits a maximum in T ( $\sim 69\%$ ) and a minimum in R ( $\sim 11\%$ ), respectively. At the laser wavelength of 633 nm T amounts to  $\sim 64\%$  and R to  $\sim 24\%$ , respectively. Additionally the simulated data of R and T are plotted in Fig. 5. A good agreement between simulated and measured spectra is achieved using layer thicknesses similar to the values estimated from the deposition rates of individual thin layers. The simulated layer stack (Structure 1) has the thickness values of the layers in the fabricated PSTD system (TCO1: 265 nm, n1: 20 nm, i1: 43 nm, p1: 42 nm, TCOm: 319 nm, n2: 22 nm, i2: 44 nm, p2: 23 nm, TCO2: 244 nm), which were deduced by fitting the calculated T and R to the measured curves using a commercial software [18]. The thickness of the individual layers estimated by the deposition rate and the data used for the simulations differ less than 15 nm, which is within the uncertainty limit of the deposition parameters. Fig. 6 (a) shows the normalized measured photocurrents of a PSTD and the normalized simulated absorbance of a structure based on the layer thicknesses derived from the former fitting. Fig. 6 (b) shows the corresponding L-curves. It demonstrates that the simulation can approximately describe the real device.  $\gamma$  of simulated Structure 1 amounts to  $109.7^\circ$ , while the fabricated PSTD exhibits a  $\gamma$  of about  $129^\circ$ . Reasons for the deviation between the experimental data and the simulations can be the following: (i) thickness uncertainty in the substrate and the thin-film layers, (ii) the employed dielectric function for the simulation might differ from the values in the detector system due to the fact that the underlying layers can affect the growth. The underlying layers are possible to alter the

dielectric function which might be different from films deposited on glass substrates. (iii) for the simulations ideal conversion of the intensity profile in the i-layers into the photocurrents have been considered. We have neglected parasitic effects such as the collection of photo-generated carriers in the doped layer and recombination losses of carriers in the i-layer.

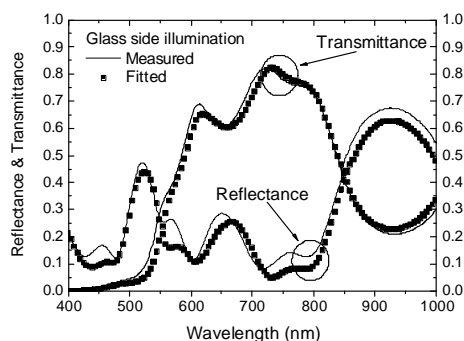


Fig. 5. Measured and simulated reflectance (R) and transmittance (T) behavior of a fabricated PSTD. The thicknesses of the layers are: TCO1: 265 nm, n1: 20 nm, i1: 43 nm, p1: 42 nm, TCOm: 319 nm, n2: 22 nm, i2: 44 nm, p2: 23 nm, and TCO2: 244 nm.

Structure 2 corresponds to the ideal thickness scheme as given in Fig. 2 – but with an increased p1-layer (TCO1: 250 nm, n1: 22 nm, i1: 44 nm, p1: 50 nm, TCOm: 333 nm, n2: 22 nm, i2: 44 nm, p2: 23 nm, TCO2: 250 nm) (see also Fig. 3 (b) and Fig. 4). The simulation demonstrates that a  $\gamma$  near  $90^\circ$  and photocurrents with low distortions are possible. The comparison of Structure 1 and Structure 2 indicates that small changes in layer thicknesses have rather high impact on the device performance, namely  $\gamma$ . For an optimization of the PSTD the deposited layers should exhibit better thickness accuracy, which is limited by the uncertainties of the production process.

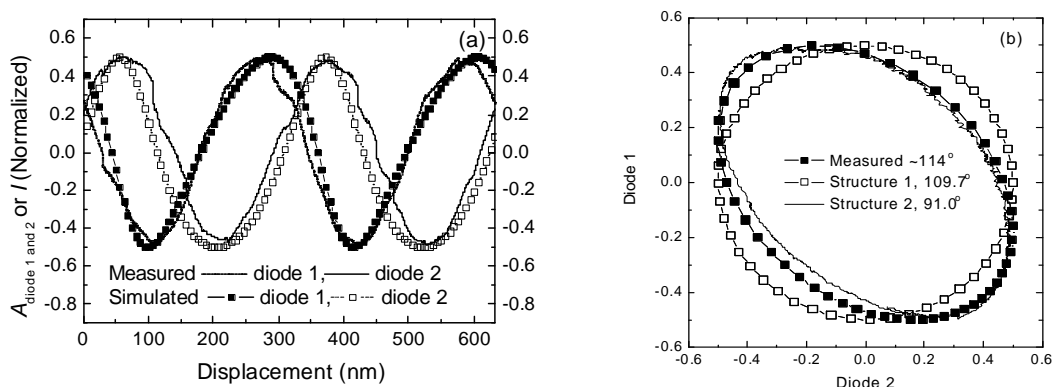


Fig. 6 (a). Normalized measured photocurrents of a PSTD and normalized absorbance of its simulation (Structure 1). The thicknesses of the layers are; TCO1: 265 nm, n1: 20 nm, i1: 43 nm, p1: 42 nm, TCOm: 319 nm, n2: 22 nm, i2: 44 nm, p2: 23 nm, and TCO2: 244 nm; (b) corresponding Lissajous curves. A simulation at an ideal thickness scheme with an increased

## 6. Outlook

For this new type of position detector the displacement of the mirror can be determined with an accuracy of up to  $\pm 15$  nm [12] using the Heydemann algorithm [19]. This is a factor of 10 - 100 higher than the values reported for state-of-the-art Michelson interferometers. The error mainly

originates from the deviation of the measured photocurrent from an ideal sine function. We have pointed out, that optical simulation can be a useful tool to achieve a better understanding of the wave propagation in these devices and thus, to develop ideal an thickness scheme that results in an improved device performance. The standing wave detector is based on an integrated detector concept. Thus, the alignment of the detector within a standing wave is easy. Therefore, the nanosensor can be used for applications where limited resolution is necessary and a low cost approach is required.

The main challenge for further improvement lies in the improvement of (i) the layer thicknesses to achieve two undisturbed sinusoidal shaped photocurrents with a  $\gamma$  of  $90^\circ$  and (ii) the cut-off frequency. Both aspects cannot be optimized independently from each other. The cut-off frequency of the device is given by the product of the capacitance and the serial resistance of the device. The latter is mainly determined by the conductivity of the TCO layers. For single n-i-p diodes a cut-off frequency between 100 and 200 kHz was achieved. A detailed capacitance-voltage (CV) analysis of thin p-i-n diodes of a-Si:H is given in [20]. The resistance of the device can be reduced by the development of an optimized contact design and the incorporation of ITO (indium tin oxide) instead of aluminium doped ZnO. In particular thin ITO layers (80 nm) have a higher conductivity than thin ZnO layers. The reduction of the serial resistance in combination with a smaller active area of the nanosensor, which will decrease the geometric capacitance of the individual diodes and will fit more appropriate with the diameter of a laser beam of 1 mm, a cut-off frequency between 500 kHz and 1 MHz should be achieved.

A further problem is the thickness control and the homogeneity of the deposited TCO and a-Si:H layers. The simulations have shown that a thickness variation of the p-layer of only 20 nm changes the shape of the L-figure from a nearly perfect circular to a straight line. Since the optical retardation between the centers of both i-layers is determined by the thickness of  $i1/2$ , p1, TCO,  $n2$  and  $i2/2$ , a small variation of the layers will result in a mismatch of  $\gamma$ . This fact demonstrates the necessity to develop a process with a high reproducibility. For both deposition techniques used - PECVD and sputtering - in-situ ellipsometry can be a useful tool for an improved process control, which could increase the accuracy and reproducibility of the thickness of the deposited layers.

To increase the yield of shunt-free devices and to decrease the capacitance we draw our attention to diodes with a thicker i-layer. Investigations of nanosensors with an i-layer thickness of  $3\lambda/(4n_{Si})$  (~130 nm) and a total diode thickness of  $3\lambda/(4n_{Si})$  (~180 nm) show that beside a reduced signal to noise ratio (ratio of the alternating component and the direct component) [12, 17] also the wave propagation in thicker diodes is more disturbed than in thin diodes. This result underlines that the whole multi-layer stack should be as thin as possible. It also indicates the potential of thin ITO contact layers for the further improvement of the new interferometer.

The realized and simulated n-i-p-diodes of the PSTD have a constant n-layer thickness. The p1-layer was enlarged experimentally to get a  $\gamma$  of  $90^\circ$ . A further step to adjust the phase between the two photocurrents is a simultaneous reduction of the n1-layer and p2-layer thickness and an increase of the n2-layer and p1-layer. In this case, the optical thickness of the whole multi-layer stack close to the ideal case (multiple of  $\lambda/(2n_{device})$ , see. Fig. 2) could be maintained and the optical retardation between the two centers of the i-layer can be tuned.

The development of a wide bandgap n-layer can be a further useful step to enhance the degree of freedom for an optical adjustment of the whole layer stack and to tune a  $\gamma$  of  $90^\circ$ , because in comparison to the n-layer used (i) the absorption losses within the n-layer can be reduced and (ii) the optical thickness of a wide bandgap material is lower. The latter one enables the incorporation of a slightly thicker n-layer to keep the optical thickness of the layer ( $n \cdot d$ ) constant and likely reduces the shunt sensitivity.

## 7. Conclusions

We have investigated the optical properties of a phase selective partly transparent detector (PSTD) by a comparison of electromagnetic simulation and experimental data. Different concepts to adjust a phasing of  $90^\circ$  between the photocurrents of both diodes were discussed. We have achieved a good agreement for the measured and simulated L-curves. Thus, the simulation predicts the photocurrents within a reliable range and shows the potential to be an useful tool for a further device optimization. Furthermore, the results show that a thicker p1-layer is a possibility to achieve photocurrents with low distortion and a  $\gamma$  near  $90^\circ$ . This leads to L-figures close to a perfect circle,

which is a prerequisite for highest measurement accuracy. Finally, further optimization criteria to improve the device performance of the interferometer like the use of thin ITO layers and an improved process control were discussed.

### Acknowledgment

The authors thank F. Finger and A. Lambertz for the support of the a-Si:H deposition, H. Siekmann and G. Schöpe for sputtering of TCO layers and H.-J. Büchner and V. Mandryka for discussion and measurements. This work was financially supported by the "Deutsche Forschungsgemeinschaft" (Sti 181/1-2).

### References

- [1] N. Bobroff, *Meas. Sci. Technol.* **4**, 907 (1993).
- [2] H. Büchner, "Stehende-Wellen-Interferometer zur Messung von optischen Gangunterschieden", Deutsches Patent DE 3300369 (1983).
- [3] M. Sasaki, X. Mi, K. Hane, *Appl. Phys. Lett.* **75**, 14, 2008 (1999).
- [4] Y. Li, X. Mi, M. Sasaki, K. Hane, *Meas. Sci. Technol.* **14**, 479 (2003).
- [5] H. L. Kung, D. A. B. Miller, P. Atanackovic, C. C. Lin, J. S. Harris, Jr., L. Carraresi, J. E. Cunningham, W. Y. Jan, *Appl. Phys. Lett.* **76**, 22, 3185-3187 (2000).
- [6] H. L. Kung, S. R. Bhalotra, J. D. Mansell, D. A. B. Miller, J. S. Harris, Jr., *IEEE Journal on selected topics in quantum electronics* **8**, 1, 98 (2002).
- [7] H. Stiebig, D. Knipp, S. Bhalotra, H.L. Kung, D.A.B. Miller, *Sensors and Actuators A* **120**, 110 (2005).
- [8] U. Gerhardt, Ph.D thesis, "Signalverarbeitung in der interferenzoptischen Meß- und Sensortechnik", University of Ilmenau, Germany (2002) ISBN: 3-932633-05-9.
- [9] H. Stiebig, H.-J. Büchner, E. Bunte, V. Mandryka, D. Knipp, G. Jäger, *Appl. Phys. Lett.* **83**, 12-14 (2003).
- [10] H. J. Büchner, E. Bunte, V. Mandryka, H. Stiebig, G. Jaeger, *Proc. SPIE Int. Soc. Opt. Eng.* **5144**, 218-226 (2003).
- [11] H. Stiebig, V. Mandryka, E. Bunte, H.-J. Büchner, K. H. Jun, G. Jäger, *J. Optoelectron. Adv. Mater.* **5**(5), 1305 (2003).
- [12] H. Stiebig, E. Bunte, K. H. Jun, "Optoelectronic Materials and Devices" vol. 1 (Non-crystalline Materials for Optoelectronics), editors: G. Lucovsky and M. Popescu, Publishing House: INOE, 417 - 440 (2004).
- [13] B. Rech, O. Kluth, T. Repmann, T. Roschek, J. Springer, J. Müller, F. Finger, H. Stiebig, H. Wagner, *Sol. Energy Mater. Sol. Cells* **74**, 439-447 (2002).
- [14] O. Kluth, A. Löffl. S. Wieder, C. Beneking, L. Houben, B. Rech, H. Wagner, S. Waser, J. A. Selvan, H. Keppner, *Proc. 26th IEEE PVSEC*, 715-718 (1997).
- [15] F. Leblanc, J. Perrin, and J. Schmitt, *J. Appl. Phys.* **75**, 1074-1087 (1994).
- [16] Z. Knittl, *Optics of thin films*, New York: Wiley 1976.
- [17] E. Bunte, V. Mandryka, K. H. Jun, H.-J. Büchner, G. Jäger, H. Stiebig, *Sensors and Actuators A* **113**, 334-337 (2004).
- [18] VASE, version 2.46 (Wollam, Lincoln, NE, 1995).
- [19] P. L. M. Heydemann, *Appl. Opt.* **20**, 3382-3384 (1981).
- [20] H. Stiebig, U. Nosan, M. Krause, M. Jankovec, M. Topic, *J. Non-Cryst. Solids* **338-340**, 772 (2004).